

UNIVERSITY OF CALIFORNIA SANTA CRUZ

PHYS 195

---

---

**Gravitational Waves and the  
Galactic Center Excess: Using  
Millisecond Pulsars to Probe  
Physics Beyond the Standard  
Model**

---

---

A UNDERGRADUATE THESIS SUBMITTED IN PARTIAL SATISFACTION  
OF THE REQUIREMENTS FOR THE DEGREE OF

BACHELOR OF SCIENCE IN PHYSICS

BY

KAYLA BARTEL

JULY 1, 2024



# Abstract

In recent years we have entered an age of multi-messenger and gravitational wave astronomy that has allowed us to study astrophysical phenomenon in new ways. This avenue of investigation into the universe has the potential to shed light on one of the enduring mysteries of high energy astrophysics: the galactic center excess. This source of gamma rays could be due to either annihilating dark matter or to a yet unresolved population of millisecond pulsars located in the Milky Way disk and the nuclear bulge. Due to their rapid rotation and strong magnetic fields, millisecond pulsars are asymmetric about their axis of rotation, causing the emission of monochromatic gravitational waves that dark matter does not emit. Using MCMC and inverse transform methods, we generate a simulated population of approximately 40,000 millisecond pulsars and their corresponding GW amplitude, luminosity, and frequency. Our results indicate that the gravitational wave frequency of a population of approximately 40,000 MSPs ranges from 200 to 1400 Hz owing to the relatively high rotational frequency of most MSPs. This limits the detectability of our signal to GW detectors capable of probing high frequency signals such as TAMA, GEO, LIGO, Virgo, Kagra, and ET. Only Advanced LIGO/Virgo (with sensitivities above  $3 \times 10^{-23}$ ), Kagra (with sensitivities above  $10^{-23}$ ), and ET (with sensitivities above  $10^{-24}$ ) are capable of detecting the GW signal, placing strong constraints on the morphology of the GW signal, the number of detectable MSPs, and the average GW frequency visible. This suggests that if MSPs are responsible for the galactic center excess, then between  $\sim 2\text{--}57$  pulsars should be detectable with a corresponding GW frequency range of 364.29–391.88 Hz and a corresponding GW luminosity range of  $2.00 \times 10^{-44}\text{--}1.05 \times 10^{-42}$ . Therefore GW detectors sensitive to gravitational waves from MSPs and thus frequencies in the hundreds of hertz, must see at least a few MSPs, otherwise there are strong constraints placed on the abilities of MSPs to contribute to the galactic center excess.

# Contents

<b>1</b>	<b>Introduction</b>	<b>6</b>
1.1	The Galactic Center Excess . . . . .	6
1.2	Millisecond Pulsars . . . . .	7
1.3	Gravitational Waves from Millisecond Pulsars . . . . .	7
1.4	Gravitational Wave Detectors . . . . .	8
1.5	Methods of Sampling . . . . .	10
1.5.1	Monte Carlo Markov Chain Sampling . . . . .	10
1.5.2	Inverse Transform Sampling . . . . .	11
1.5.3	Sampling a 2D Distribution . . . . .	11
<b>2</b>	<b>Sampling the Millisecond Pulsar Population</b>	<b>12</b>
2.1	Millisecond Pulsar Densities in the Milky Way . . . . .	12
2.2	Sampling the Pulsar Population . . . . .	13
<b>3</b>	<b>Ellipticity Distribution of Millisecond Pulsars</b>	<b>19</b>
<b>4</b>	<b>Generating the Gravitational Wave Signal</b>	<b>23</b>
<b>5</b>	<b>Analysis and Possibility of Detection</b>	<b>25</b>
<b>6</b>	<b>Conclusion</b>	<b>28</b>
<b>7</b>	<b>Acknowledgements</b>	<b>29</b>
<b>8</b>	<b>References</b>	<b>30</b>

## List of Figures

1	A diagram of the type of laser interferometer used in gravitational wave detectors, specifically depicting the Advanced LIGO Detector [1]. A 1064 nm Nd:YAG laser beam is spit down two arm cavities of length 4 km [1]. . . . .	9
2	A colormap of the MSP density distribution in the Milky Way disk. The density significantly decreases for $z \gtrsim 1000$ pc and $R \gtrsim 5000$ pc, producing a oblong, oval shape. . . . .	12
3	A colormap of the MSP density distribution in the Milky Way nuclear bulge. The density decays rapidly causing a highly localized star-shaped distribution located at the origin. . . . .	13
4	Comparison of the Milky Way Disk density and the corresponding sample generated by MCMC methods. The generated sampled of MSPs follows the same decay pattern and thus has a similar shape to the density distribution, as seen by it's agreement with the contours in (b). . . . .	14
5	A comparison between the sampled first piece of the NSC density and the function itself, generated using MCMC methods. The sample (blue histogram) shows good correlation with the sampled function, here shown in orange. . . . .	15
6	A comparison between the sampled second piece of the NSC density and the function itself, generated using MCMC methods. The sample (blue histogram) shows good correlation with the sampled function, here shown in red. . . . .	15
7	A comparison between the sampled z values of the NSD density and the function itself, generated using MCMC methods. The sample (blue histogram) shows good correlation with the sampled function, here shown in purple. . . . .	16
8	A comparison between the sampled first piece of the NSD density and the function itself, generated using MCMC methods. The sample (blue histogram) shows good correlation with the sampled function, here shown in gray. . . . .	17
9	Comparison of the second piece of the NSD radial density to its inverse CDF. . . . .	18
10	A comparison between the sampled second piece of the NSD density and the function itself, using Inverse Transform methods. The sample (green histogram) shows good correlation with the sampled function, here shown in pink. . . . .	18

11	Comparison of the third piece of the NSD radial density to its inverse CDF. . . . .	19
12	A comparison between the sampled third piece of the NSD density and the function itself, using Inverse Transform Methods. The sample (aqua histogram) shows good correlation with the sampled function, here shown in red. . . . .	19
13	The probability density of the external magnetic fields for MSPs; a log-normal distribution with $\log_{10}(B_{med}) = 8.21$ , with $B_{med}$ in G, and $\sigma_B = 0.21$ . . . . .	20
14	The inverse CDF of MSP external magnetic fields. . . . .	20
15	A histogram of the external magnetic fields of millisecond pulsars. . . . .	21
16	A histogram of the internal magnetic fields of millisecond pulsars. . . . .	21
17	A histogram of the ellipticities of millisecond pulsars, derived from the internal magnetic field. . . . .	22
18	One generation of an Aitoff projection of the locations and ellipticities of sampled millisecond pulsars. . . . .	22
19	A histogram of the $\log_{10}$ GW amplitude of MW sampled millisecond pulsars. Most have amplitudes of $\sim 10^{-27}$ – $10^{-30}$ , with a smaller number having amplitudes greater than $10^{-26}$ but less than $10^{-22}$ . . . . .	23
20	One generation of an Aitoff projection of a sampled of MW millisecond pulsars with corresponding $\log_{10}$ GW amplitude. . . . .	23
21	A histogram of the $\log_{10}$ GW frequency of MW sampled millisecond pulsars. Most MSPs have a GW frequency in the range of $\sim 200$ to $1400$ Hz. . . . .	24
22	One generation of an Aitoff projection of a sampled of MW millisecond pulsars with corresponding $\log_{10}$ GW luminosity. . . . .	24
23	One generation of a Mollweide projection of a sampled of MW millisecond pulsars with corresponding $\log_{10}$ GW luminosity, smoothed with an angular resolution of 1 arc-minute. . . . .	25
24	A depiction of the sensitivity curves of various gravitational wave detectors [23]. The detectors capable of detecting frequencies in the $10^2$ – $10^3$ Hz range, TAMA, GEO, LIGO, Virgo, Kagra, and ET, are marked in an array of colors. . . . .	25
25	The GW signal for 1.7 degree angular resolution, with no sensitivity constraints enforced. . . . .	26
26	The GW signal for 1.7 degree angular resolution, with conservative sensitivity constraints enforced. . . . .	26

27	The GW signal for 1.7 degree angular resolution, with optimal sensitivity constraints enforced. . . . .	26
28	The GW signal for 10 degree angular resolution, with no sensitivity constraints enforced. . . . .	27
29	The GW signal for 10 degree angular resolution, with conservative sensitivity constraints enforced. . . . .	27
30	The GW signal for 10 degree angular resolution, with optimal sensitivity constraints enforced. . . . .	27
31	A histogram of the number of MSPs detectable for the most conservative GW detector sensitivity bounds. . . . .	27
32	A histogram of the average GW frequency from detectable MSPs for the most conservative GW detector sensitivity bounds.	27
33	A histogram of the average GW luminosity from detectable MSPs for the most conservative GW detector sensitivity bounds.	27
34	A histogram of the number of MSPs detectable for the most optimal GW detector sensitivity bounds. . . . .	28
35	A histogram of the average GW frequency from detectable MSPs for the most optimal GW detector sensitivity bounds. .	28
36	A histogram of the average GW luminosity from detectable MSPs for the most optimal GW detector sensitivity bounds. .	28

# 1 Introduction

In recent years, we have entered an age of multi-messenger astrophysics. This is especially apparent in the field of gravitational wave astronomy, allowing researchers to probe new phenomena and old mysteries alike. One of the most enduring astrophysical mysteries is that of the Galactic Center Excess, upon which the following discussion is based.

## 1.1 The Galactic Center Excess

The Galactic Center Excess (GCE) is a source of high energy gamma rays (1-3 GeV) located in the center of the Milky Way Galaxy, discovered by the Large Area Telescope (LAT) on board the Fermi Gamma-ray Space Telescope [14, 27]. Models have shown that the GCE is either spherical or bulge-like in shape, with each morphology corresponding to a different origin [27].

If the GCE is considered to be a spherical source of gamma rays, then it can be argued that the GCE is caused by annihilating dark matter (DM). The corresponding gamma ray spectrum's shape, resembling the square of a steepened Navarro-Frenk-White (NFW) profile, could suggest a  $\lesssim 100$  GeV thermal relic DM annihilating to quarks [27].

However, it is impossible to rule out the possibility of other astrophysical point sources with a similar spectral shape and morphology, especially assuming the GCE has a bulge-like shape [27]. In fact, several authors posit that the GCE is caused by an unresolved population of millisecond pulsars (MSPs), with many models fitting the morphology and energetics of the GCE remarkably well [12, 24].

There is some ambiguity in the determination of the shape of the GCE, as it depends heavily on the model of the continuum gamma-ray backgrounds used. Both GALPROP [19, 20] and SkyFACT [28] suggest a bulge-like morphology, though due to uncertainty in current interstellar gas maps and the background models themselves, the ambiguity remains. Another method of determining the cause of the GCE is studying photon statistics: a DM signal would produce a smooth spatial distribution of flux while pulsars would produce more concentrated distributions [27]. Recent studies are conflicted, suggesting both that there is some evidence for point sources [9] and that the GCE is an asymmetric smooth emission [17, 18].

With the help of other methods of inquiry into this question, such as determining the gravitational wave signal generated by MSPs, this ambiguity has the potential to be lifted. Such an investigation is the focus of the

following work.

## 1.2 Millisecond Pulsars

MSPs are rapidly rotating neutron stars with rotation periods in the milliseconds whose rotational frequency has been accelerated by accreting mass from a companion star. MSPs are found in the interstellar medium, as well as in globular clusters and galactic bulges [12]. Millisecond pulsars emit curvature radiation in the form of radio and gamma rays, driven by the motion of charged particles along strong magnetic field lines. These emissions are not isotropic, instead the strongest emission is along the magnetic axis—reminiscent of a lighthouse [24].

These external magnetic fields ( $\sim 10^8 - 10^9$  G) can cause the MSP to spin down due to magnetic dipole braking, though, MSPs spin down more slowly compared to young pulsars, as a result of their weaker magnetic fields. Millisecond pulsars are thus a more likely candidate for the GCE—younger pulsars would have spun down to a point where their gamma ray emissions aren't sufficient to produce the appropriate GCE signal [24].

We model the probability density of the external magnetic field of a millisecond pulsar with a log-normal distribution, given by [24]:

$$p(\log_{10}(B)|B_{med}, \sigma_B) = \frac{1}{\sqrt{2\pi}\sigma_B} \exp\left(-\frac{(\log_{10}(B) - \log_{10}(B_{med}))^2}{2\sigma_B^2}\right) \quad (1)$$

with  $\log_{10}(B_{med}) = 8.21$ , with  $B_{med}$  in G, and  $\sigma_B = 0.21$ . This model gives a good fit to the Fermi-LAT MSP histogrammed data [24].

## 1.3 Gravitational Waves from Millisecond Pulsars

The theory of general relativity posits that gravitational waves (GW), perturbations in the fabric of space-time traveling at the speed of light, exist. Their existence is further supported by both direct and indirect observational evidence. These distortions were first observed via the detection of the binary star merger GW170817 by LIGO in 2017 [3]. Due to conservation of mass and conservation of momentum, emission from the monopole and dipole is impossible. Therefore, the lowest radiating multipole is the quadrupole [26].

In the case of millisecond pulsars, monochromatic gravitational waves can be emitted due to asymmetric deformations of the pulsar around the

axis of rotation [5]. One such cause of these deformations is a strong internal magnetic field,  $B_{int}$ , provided the field does not align with the axis of rotation [22].

This axial asymmetry can be written in terms of the dimensionless equatorial ellipticity,  $\epsilon$ , which is proportional to the GW strain amplitude [5]. The ellipticity is defined in relation to the star's principle moments of inertia  $I_{xx}, I_{yy}, I_{zz}$  [22]:

$$\epsilon = \frac{|I_{xx} - I_{yy}|}{I_{zz}} \quad (2)$$

In practice,  $|\epsilon| \ll 1$ ,  $I_{xx} \simeq I_{yy} \simeq I_{zz} = I$ , with a conservative estimate for  $I$  being  $1.1 \times 10^{38} \text{ kg m}^2$ . Assuming a superconducting core, we can model the ellipticity as [22]:

$$\epsilon \approx 10^{-8} \left( \frac{B_{int}}{10^{12}} \right) \quad (3)$$

However, the internal magnetic field isn't observable directly. Instead we must infer it from the MSP's external magnetic field,  $B_{ext}$ , using  $B_{int} = 150B_{ext}$  [22]. This is a conservative estimate, as the internal magnetic field could be as much as  $10^4$  times larger than the external magnetic field [22].

The gravitational wave amplitude  $h_0$  is then given by [22]:

$$h_0 = \frac{16\pi^2 G}{c^4} \frac{I_{zz}\epsilon f_{rot}^2}{d} \quad (4)$$

with  $d$  the distance to the MSP from Earth,  $f_{rot}$  the MSP's rotational frequency, and  $G$  the gravitational constant.

## 1.4 Gravitational Wave Detectors

All operational gravitational wave detectors, such as LIGO, Virgo, GEO, TAMA, and Kagra, use laser interferometry to detect gravitational waves [1, 4, 11, 6, 7]. Figure 1 depicts a typical layout for a laser interferometer.

Laser interferometers work based on the principle of interference. A coherent beam of light is passed through a beam splitter and is split down both arms of the interferometer. Differential movement of the arms changes the optical path length and induces a 180 degree phase difference between the two beams of light, causing constructive interference proportional to the GW strain [2].

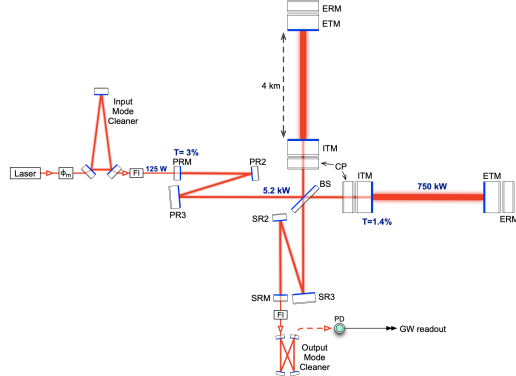


Figure 1: A diagram of the type of laser interferometer used in gravitational wave detectors, specifically depicting the Advanced LIGO Detector [1]. A 1064 nm Nd:YAG laser beam is split down two arm cavities of length 4 km [1].

Gravitational waves are transverse–oscillations occur orthogonal to the direction of propagation. Consequently, when a gravitational wave distorts space-time, one transverse direction is contracted while the direction orthogonal to the transverse plane is expanded, causing differential motion of the interferometer arms and detection of the gravitational wave [2].

Certain detectors, such as TAMA and GEO, and upgraded detectors such as advanced LIGO and advanced Virgo, use a modified design called a Fabry-Perot-Michelson interferometer with power and signal recycling cavities located in the arms of the detector [25]. This allows detectors such as TAMA and GEO to have much shorter arm lengths of 300m and 600m respectively [6], while allowing other detectors enhanced power and the ability to shape the signal response [25]. In both cases, the usual arms of the Michelson interferometer are replaced with Fabry-Perot arm cavities producing a more compact and efficient design than other GW detectors [6].

Several other designs for gravitational wave detectors have been proposed in recent years, such as Einstein Telescope [25], as well as upgrades to existing GW detectors such as GEO—to increase the sensitivity to up to 600 Hz [11].

The Einstein Telescope is composed of three gravitational wave detectors based on current Fabry-Perot-Michelson interferometers, in the shape of an equilateral triangle, with each arm containing a low frequency (3-30 Hz) detector and a high frequency (30 Hz-10 kHz) detector [25]. The Fabry-Perot cavities are designed to have large beam sizes, combating the impact

of thermal noise from the optics on the detector sensitivity [25].

## 1.5 Methods of Sampling

To model the relevant parameters in the following work, two methods of generating samples were used: Monte Carlo Markov Chain sampling and Inverse Transform sampling.

### 1.5.1 Monte Carlo Markov Chain Sampling

Monte Carlo Markov Chain sampling (MCMC) is a method for generating a sample of the required parameter  $x_1, x_2, \dots, x_n$  that follows a distribution  $p(x)$ , for a sufficiently large sample size [24]. In particular, a version of Goodman and Weare's Affine Invariant MCMC Ensemble sampler was used [13].

A typical MCMC sampler undergoes an iterative procedure where, starting with an initial position, a new proposed position sampled from a transition distribution is accepted with some defined probability. If the step is accepted and saved, the process repeats with a new initial position, and if not, the initial position is saved and the process repeats [13].

The sampler proposed by Goodman and Weare is a significantly more efficient version, simultaneously evolving N walkers in an ensemble to explore the parameter space and generate samples. The proposal distribution for a single walker is based on the current positions of the remaining N - 1 walkers. To advance one walker to a new position from position  $X_n$ , a walker  $X_j$  is randomly chosen from the remaining pool and a new position:

$$X_n(t) \rightarrow Y = X_j + Z[X_n(t) - X_j] \quad (5)$$

is proposed, with Z a random variable drawn from a distribution:

$$g(Z = z) \propto \begin{cases} \frac{1}{\sqrt{z}} & \text{if } z \in [\frac{1}{a}, a] \\ 0 & \text{otherwise} \end{cases} \quad (6)$$

where a is an adjustable scale parameter, set to 2 for the following work [13].

The proposal will be accepted according to the probability:

$$q = \min \left( 1, Z^{N-1} \frac{P(Y)}{P(X_n(t))} \right) \quad (7)$$

where N is the dimension of the parameter space. This process is then repeated for each walker in the ensemble in series until a sample is generated [13].

### 1.5.2 Inverse Transform Sampling

Inverse Transform Sampling is another way to sample from a certain distribution  $p(x)$ , provided its cumulative distribution function (CDF), given by:

$$CDF(x) = \int_{-\infty}^{x'} p(x') dx' \quad (8)$$

The CDF, evaluated at  $y$ , represents the probability that  $p(x)$  will take a value less than or equal to  $y$ . Upon inversion, the inverse CDF,  $I_{CDF}(x) = CDF^{-1}(x)$ , can be used to generate a value from  $p(x)$  when given an input in the range  $[0, 1]$  [16].

### 1.5.3 Sampling a 2D Distribution

Sampling a 2D function,  $f(x, y)$ , requires splitting the function into two conditional functions,  $f(x|y)$  and  $f(y|x)$ , as the MCMC and Inverse Transform Sampling methods discussed in Sections 1.5.1 and 1.5.2 are 1-dimensional. The conditional function  $f(x|y)$  is a function of only  $x$ , given by:

$$f(x|y) = \frac{f(x, y)}{f_y(y)} = \frac{f(x, y)}{\int_{-\infty}^{\infty} f(x', y) dx'} \quad (9)$$

Similarly, the conditional function  $f(y|x)$  is a function of only  $y$ , given by:

$$f(y|x) = \frac{f(x, y)}{f_x(x)} = \frac{f(x, y)}{\int_{-\infty}^{\infty} f(x, y') dy'} \quad (10)$$

For piece-wise functions  $f(x,y)$ , the integral bounds for  $f_x(x)$  and  $f_y(y)$  are given by the piece-wise bounds. Either MCMC or Inverse Transform sampling can be carried out on  $f(x|y)$  and  $f(y|x)$  to find the corresponding distributions of  $x$  and  $y$  that follow the function  $f(x, y)$ .

Section 2 discusses the MSP population models and methods used to generate a sample from the millisecond pulsar population, Section 3 discusses the ellipticity distribution of our population of sampled MSPs, Section 4 covers the gravitational wave signal generated by our population of millisecond pulsars, Section 5 discusses our results and compares the generated GW signal to current and future detector sensitivities, and Section 6 covers our concluding remarks and future work.

## 2 Sampling the Millisecond Pulsar Population

### 2.1 Millisecond Pulsar Densities in the Milky Way

Two MSP density distributions were used to generate a population of MSPs in the Galactic Center: a disk distribution and a nuclear bulge distribution. The disk distribution is of the form:

$$\rho_{\text{disk}}(R, z) = \frac{N_{\text{disk}} M_{\odot}}{4\pi\sigma_r^2 z_0} \exp\left(\frac{-R^2}{2\sigma_r^2}\right) \exp\left(\frac{-|z|}{z_0}\right) \quad (11)$$

with  $R^2 = x^2 + y^2$  is the radial coordinate in the Galactic disk and  $z$  is the height above the Galactic plane [24].  $\sigma_r$  and  $z_0$  were chosen to be 4500 pc and 710 pc respectively in accordance with [24].  $N_{\text{disk}}$  is the number of MSPs in the Milky Way disk, and was chosen to be 6000 stars [30]. See Figure 2 for a plot of the MSP disk distribution.

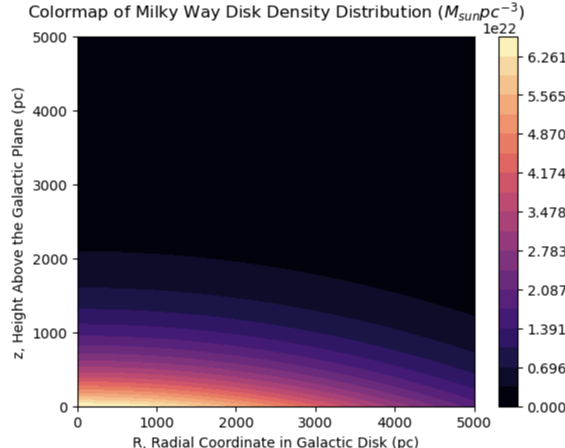


Figure 2: A colormap of the MSP density distribution in the Milky Way disk. The density significantly decreases for  $z \gtrsim 1000$  pc and  $R \gtrsim 5000$  pc, producing an oblong, oval shape.

The nuclear bulge distribution is split into two separate populations, that of the nuclear stellar cluster (NSC) and that of the nuclear stellar disk:

$$\rho_{\text{nuclear bulge}}(r, z) = \rho_{\text{NSC}}(r) + \rho_{\text{NSD}}(r, z) \quad (12)$$

with  $r^2 = x^2 + y^2 + z^2$  [24]. The nuclear stellar cluster has the density:

$$\rho_{\text{NSC}}(r) = \begin{cases} \frac{\rho_0, \text{ NSC}}{1 + \left(\frac{r}{r_0}\right)^2} & r \leq 6 \text{ pc} \\ \frac{\rho_1, \text{ NSC}}{1 + \left(\frac{r}{r_0}\right)^3} & 6 \text{ pc} < r \leq 200 \text{ pc} \\ 0 & r > 200 \text{ pc} \end{cases} \quad (13)$$

with  $r_0 = 0.22 \text{ pc}$ ,  $\rho_0, \text{ NSC} = 3.3 \times 10^6 M_\odot \text{pc}^{-3}$ , and  $\rho_1, \text{ NSC} = 8.9 \times 10^7 M_\odot \text{pc}^{-3}$  [24]. The nuclear stellar disk distribution is given by:

$$\rho_{\text{NSD}}(r, z) = \begin{cases} \rho_0, \text{ NSD} r^{-0.1} \exp \frac{-|z|}{45} & r < 120 \text{ pc} \\ \rho_1, \text{ NSD} r^{-3.5} \exp \frac{-|z|}{45} & 120 \text{ pc} \leq r < 220 \text{ pc} \\ \rho_2, \text{ NSD} r^{-10} \exp \frac{-|z|}{45} & r \geq 220 \text{ pc} \end{cases} \quad (14)$$

with  $\rho_0, \text{ NSD} = 301 M_\odot \text{pc}^{-3}$ ,  $\rho_1, \text{ NSD} = 3.53 \times 10^9 M_\odot \text{pc}^{-3}$ , and  $\rho_2, \text{ NSD} = 5.94 \times 10^{24} M_\odot \text{pc}^{-3}$  [24]. See Figure 3 for a plot of the nuclear bulge distribution.

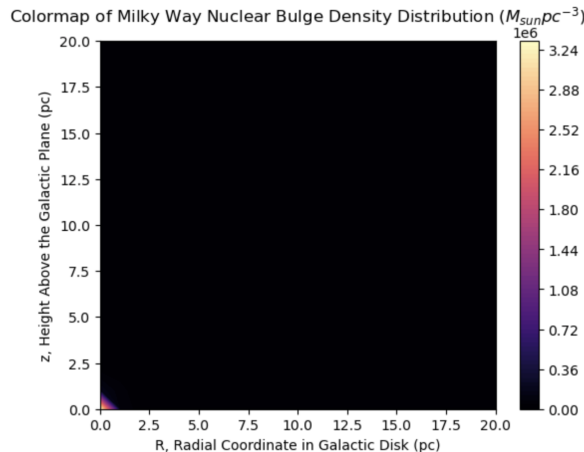


Figure 3: A colormap of the MSP density distribution in the Milky Way nuclear bulge. The density decays rapidly causing a highly localized star-shaped distribution located at the origin.

## 2.2 Sampling the Pulsar Population

To sample the Milky Way disk population, emcee, a MCMC package written in Python was used [13]. For the MW Disk population, MCMC sampling was used to sample the corresponding conditional functions, given as:

$$\rho(z|R) = \frac{1}{2z_0} \exp\left(\frac{-|z|}{z_0}\right) \quad (15)$$

and:

$$\rho(R|z) = \frac{1}{2\pi\sigma_R^2} \exp\left(\frac{-R^2}{2\sigma_R^2}\right) \quad (16)$$

with  $z$ ,  $r$ ,  $z_0, \sigma_R$  defined as in equation 11. A comparison between the generated sample, plotted as a 2D histogram, and equation 11, plotted as a contour map, can be seen in Figure 4.

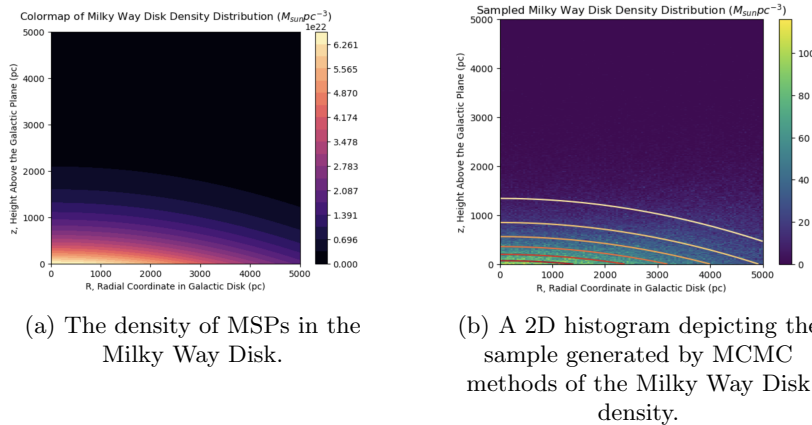


Figure 4: Comparison of the Milky Way Disk density and the corresponding sample generated by MCMC methods. The generated sample of MSPs follows the same decay pattern and thus has a similar shape to the density distribution, as seen by its agreement with the contours in (b).

The nuclear bulge populations were sampled using both MCMC and Inverse Transform methods as certain pieces of the nuclear bulge population, being rapidly decaying power laws, resulted in the MCMC algorithm ineffectively exploring the appropriate range of parameter space. For such pieces, Inverse Transform Sampling was used.

The NSC density, consisting of the two equations given in equation 13, was sampled using MCMC methods. See Figures 5 and 6 for a comparison between the MCMC generated sample and the function itself.

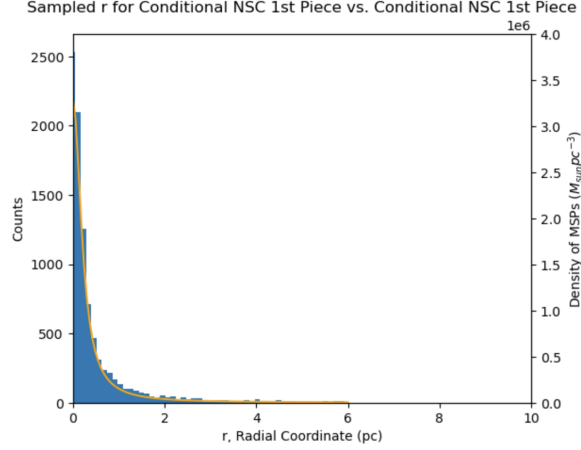


Figure 5: A comparison between the sampled first piece of the NSC density and the function itself, generated using MCMC methods. The sample (blue histogram) shows good correlation with the sampled function, here shown in orange.

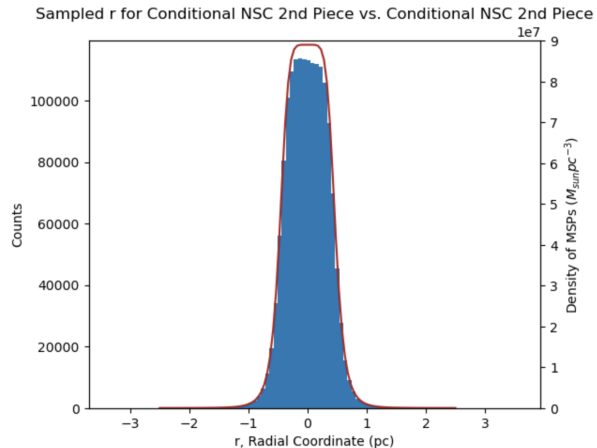


Figure 6: A comparison between the sampled second piece of the NSC density and the function itself, generated using MCMC methods. The sample (blue histogram) shows good correlation with the sampled function, here shown in red.

In addition to the NSC population, MCMC methods were used to sample parts of the NSD population. The following conditional functions were

sampled:

$$\rho_{\text{NSD}}(z|r) = \frac{1}{90} \exp\left(\frac{-|z|}{45}\right) \quad (17)$$

and

$$\rho_{\text{NSD}, 1}(r|z) = 0.0121r^{-0.1} \quad (18)$$

with 18 in the range of [0, 120], and z, r as defined in equation 14. See Figures 7 and 8 for a comparison.

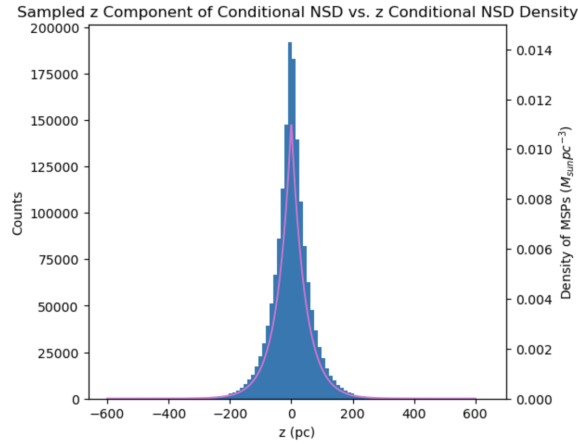


Figure 7: A comparison between the sampled z values of the NSD density and the function itself, generated using MCMC methods. The sample (blue histogram) shows good correlation with the sampled function, here shown in purple.

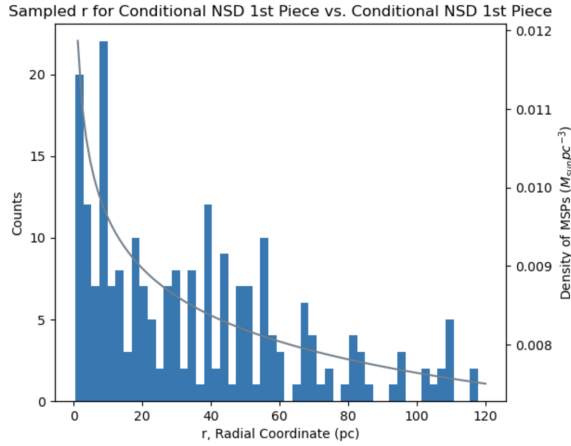


Figure 8: A comparison between the sampled first piece of the NSD density and the function itself, generated using MCMC methods. The sample (blue histogram) shows good correlation with the sampled function, here shown in gray.

The last pieces of the NSD population were sampled using Inverse Transform methods. The general form of the inverse CDF for a power law of the form  $f(x) = cx^{-a}$  given between two bounds  $[x_0, x_1]$  is:

$$CDF^{-1}(x) = [(x_1^{1-a} - x_0^{1-a})y + x_0^{1-a}]^{\frac{1}{1-a}} \quad (19)$$

with  $a = 3.5$ ,  $x_0 = 120$  pc, and  $x_1 = 220$  pc for the 2nd piece of the radial density in the NSD and  $a = 10$ ,  $x_0 = 220$  pc, and  $x_1 = 500$  pc for the 3rd piece of the radial density in the NSD.

For a comparison of the second piece of the radial density in the NSD to its CDF and the generated sample, see Figures 9 and 10. Similarly, for the third piece, see Figures 11 and 12.

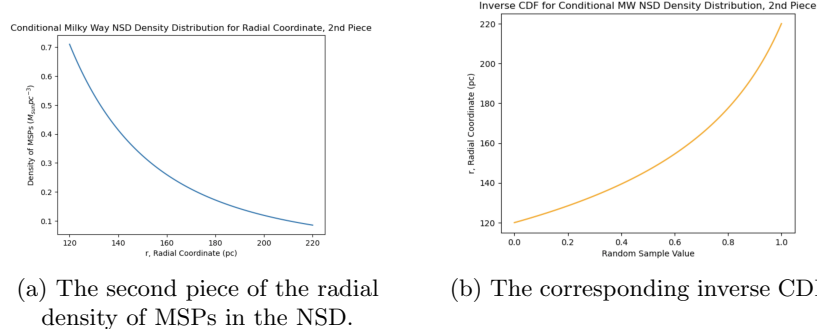


Figure 9: Comparison of the second piece of the NSD radial density to its inverse CDF.

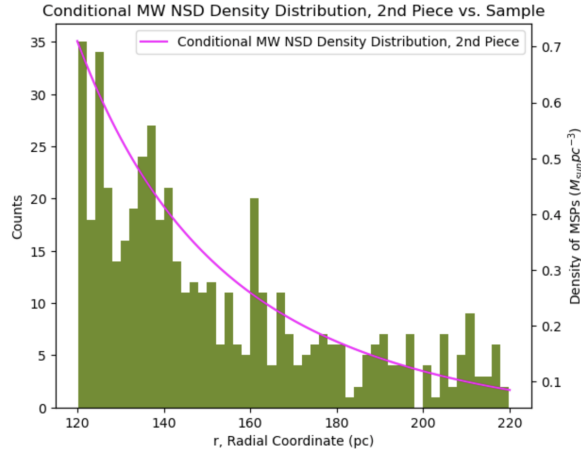


Figure 10: A comparison between the sampled second piece of the NSD density and the function itself, using Inverse Transform methods. The sample (green histogram) shows good correlation with the sampled function, here shown in pink.

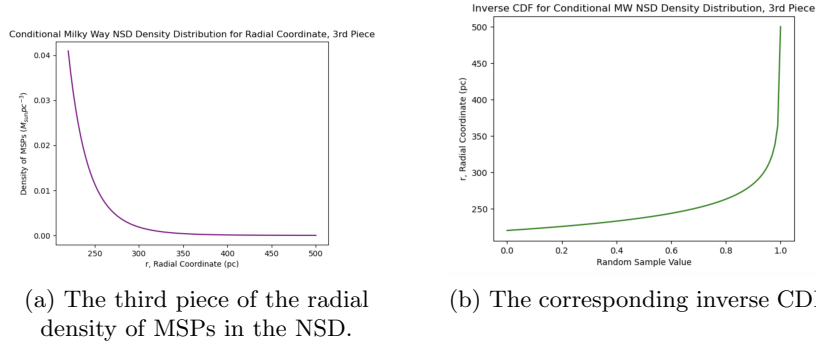


Figure 11: Comparison of the third piece of the NSD radial density to its inverse CDF.

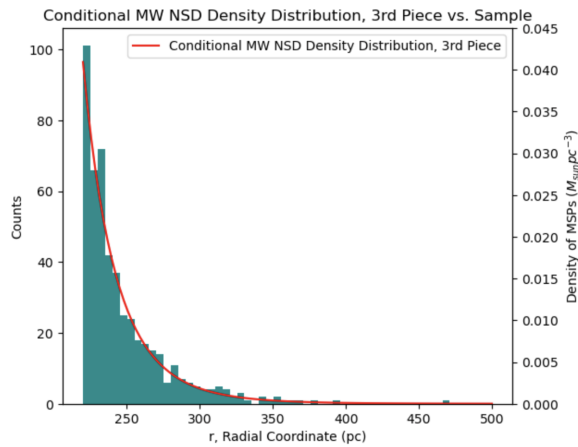


Figure 12: A comparison between the sampled third piece of the NSD density and the function itself, using Inverse Transform Methods. The sample (aqua histogram) shows good correlation with the sampled function, here shown in red.

### 3 Ellipticity Distribution of Millisecond Pulsars

To determine the ellipticity distribution of MSPs in the Milky Way, a method similar to Miller et al. [22] was used, with the probability distribution of the external magnetic fields given by Equation 1. See Figure 13 for a plot of the aforementioned probability.

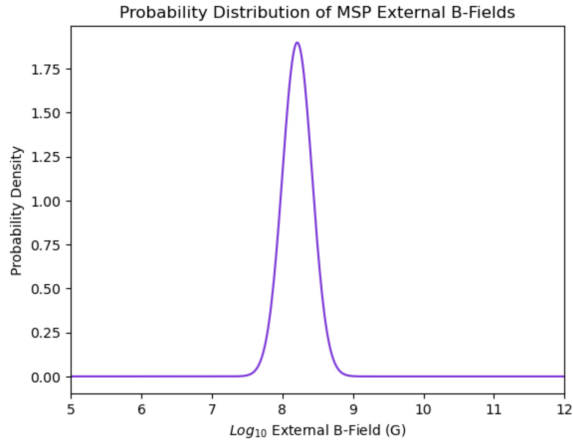


Figure 13: The probability density of the external magnetic fields for MSPs; a log-normal distribution with  $\log_{10}(B_{med}) = 8.21$ , with  $B_{med}$  in G, and  $\sigma_B = 0.21$ .

To generate a sample of external magnetic field values for the MSP populations, Inverse Transform sampling was used, resulting in the CDF shown in Figure 14 and a sample shown in Figure 15.

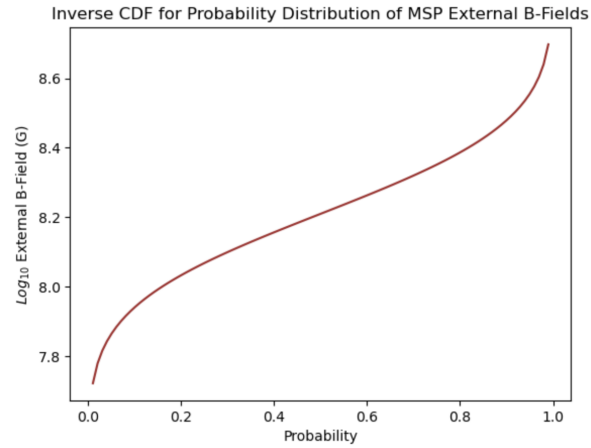


Figure 14: The inverse CDF of MSP external magnetic fields.

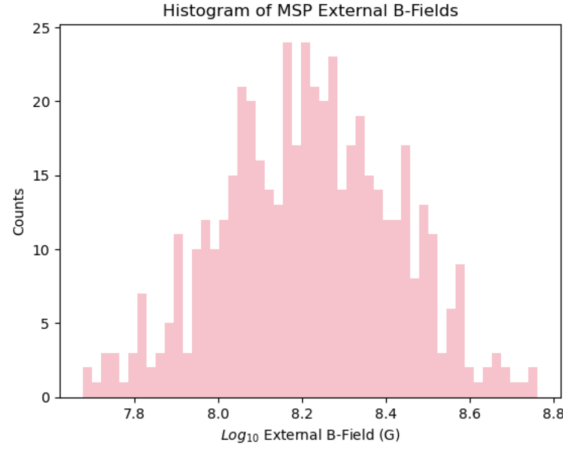


Figure 15: A histogram of the external magnetic fields of millisecond pulsars.

The corresponding internal magnetic fields were then found from the external magnetic field distribution using  $B_{int} = 150B_{ext}$ , shown in Figure 16.

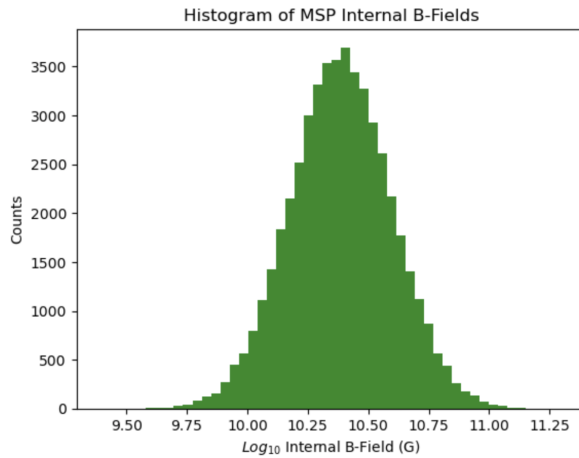


Figure 16: A histogram of the internal magnetic fields of millisecond pulsars.

This resulted in a distribution of ellipticity values, given by equation 2, and shown in Figure 17.

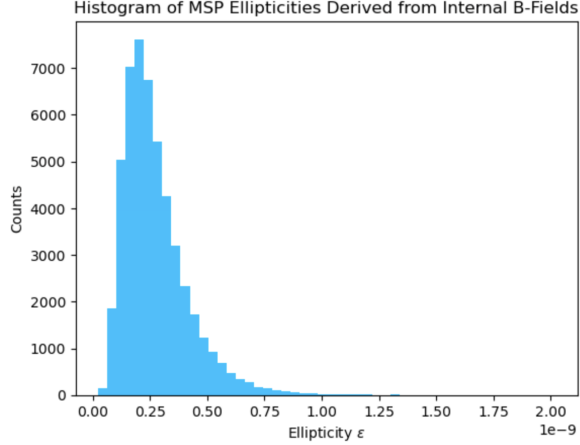


Figure 17: A histogram of the ellipticities of millisecond pulsars, derived from the internal magnetic field.

The resultant ellipticity distribution is within minimum ellipticity ranges described by Woan et al. [29] and Chen et al. [10] of  $\epsilon \approx 10^{-9}$ , and agrees with the values obtained by Miller et al. [22]. Plotting a sample of approximately 40,000 MSPs, to be within constraints given by Holst et al. [15], with a randomly drawn sample from the ellipticity distribution results in Figure 18.

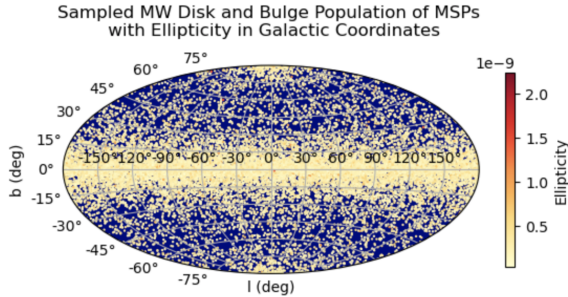


Figure 18: One generation of an Aitoff projection of the locations and ellipticities of sampled millisecond pulsars.

## 4 Generating the Gravitational Wave Signal

Calculating the GW amplitude using Equation 4 requires a MSP rotational frequency distribution. This was derived from the ATNF Pulsar Catalog [21] and modeled using a Gaussian distribution with  $\mu = 288.2$  and  $\sigma = 121.4$ . MSPs were assumed to have a frequency of over 100 Hz. The resultant GW amplitude distribution is plotted in Figure 19 in log scale.

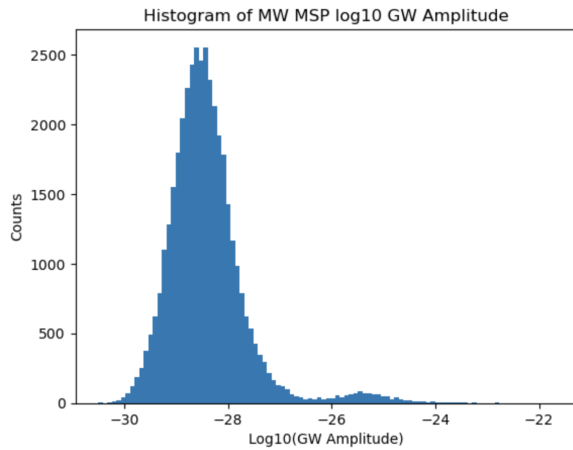


Figure 19: A histogram of the  $\log_{10}$  GW amplitude of MW sampled millisecond pulsars. Most have amplitudes of  $\sim 10^{-27}$ – $10^{-30}$ , with a smaller number having amplitudes greater than  $10^{-26}$  but less than  $10^{-22}$ .

A plot of the sampled MSP spatial distribution with corresponding GW amplitude values in log scale is shown in Figure 20.

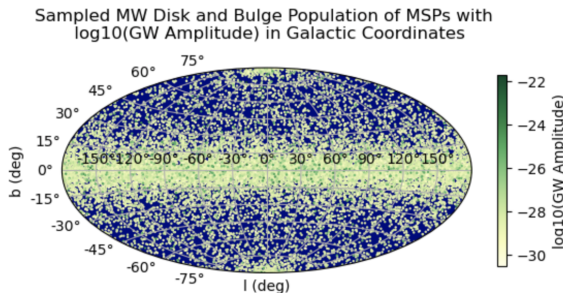


Figure 20: One generation of an Aitoff projection of a sampled of MW millisecond pulsars with corresponding  $\log_{10}$  GW amplitude.

The gravitational wave frequency of the MSPs was also calculated using  $f_{GW} = 2f_{rot}$  as in Miller et al. [22], resulting in Figure 21.

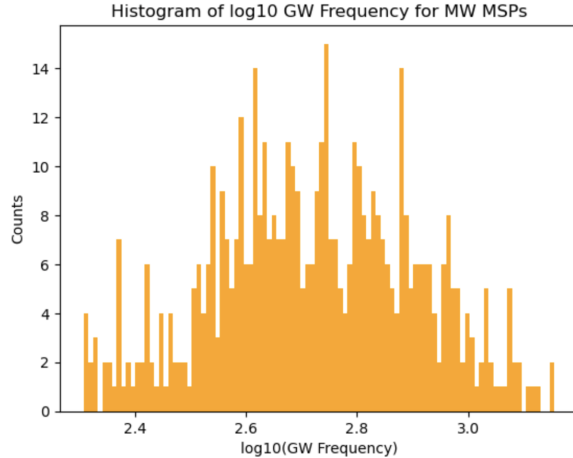


Figure 21: A histogram of the log 10 GW frequency of MW sampled millisecond pulsars. Most MSPs have a GW frequency in the range of  $\sim 200$  to 1400 Hz.

Squaring the GW amplitude results in the GW luminosity, as seen in Figure 22, plotted in log base 10.

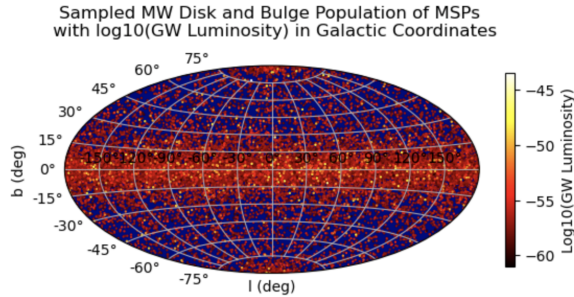


Figure 22: One generation of an Aitoff projection of a sampled of MW millisecond pulsars with corresponding log10 GW luminosity.

This was then smoothed using the angular resolution (1 arc-minute) of the future gravitational wave detector ALIA [8]. The corresponding log scale GW luminosity is seen in Figure 23.

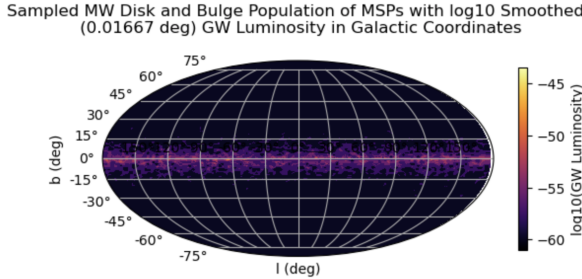


Figure 23: One generation of a Mollweide projection of a sampled of MW millisecond pulsars with corresponding  $\log_{10}$  GW luminosity, smoothed with an angular resolution of 1 arc-minute.

## 5 Analysis and Possibility of Detection

Our results indicate that the gravitational wave frequency of a population of approximately 40,000 MSPs ranges from 2.3 to 3.5 in log space, or approximately 200 to 1400 Hz, owing to the relatively high rotational frequency of most MSPs. This limits the detectability of our signal to GW detectors capable of probing high frequency signals. Consulting with a depiction of the sensitivities of most current and planned GW observatories in Figure 24, it becomes apparent that only detectors such as TAMA, GEO, LIGO, Virgo, Kagra, and ET are capable of detecting such a signal.

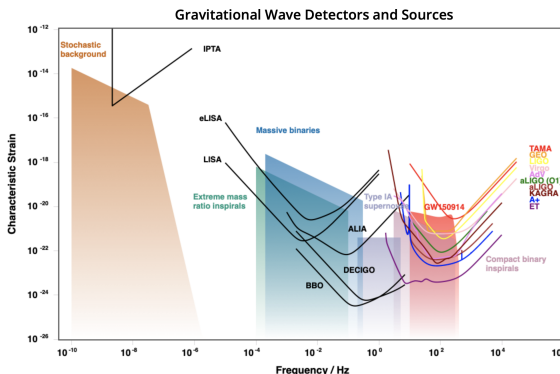


Figure 24: A depiction of the sensitivity curves of various gravitational wave detectors [23]. The detectors capable of detecting frequencies in the  $10^2$ – $10^3$  Hz range, TAMA, GEO, LIGO, Virgo, Kagra, and ET, are marked in an array of colors.

These detectors correspond to an ability to detect the characteristic strain, or GW amplitude, in a particular range, placing further constraints on the GW signal we model. Figure 19 indicates that all GW amplitude values are below  $10^{-22}$ , suggesting that only Advanced LIGO/Virgo (with sensitivities above  $3 \times 10^{-23}$ ), Kagra (with sensitivities above  $10^{-23}$ ), and ET (with sensitivities above  $10^{-24}$ ) would be capable of detecting the GW signal.

With these limitations in mind, the GW signal was adapted to exclude GW amplitudes smaller than  $3 \times 10^{-23}$  (conservatively) and GW amplitudes smaller than  $10^{-24}$  (optimistically). In addition, smoothing of the GW signal was adapted to better reflect that the angular resolution of most GW detectors is quite poor, limited to between tens and hundreds of square degrees [8]. A range of 1 arcminute, 10 arcminutes, 1 deg, and 10 degrees were plotted for both limitations of GW detector sensitivities.

The most conservative sensitivity bounds and the smallest angular resolutions of 1 and 10 arcminute(s) compounded to produce no detectable signal. A slightly larger angular resolution of 1.7 degrees still resulted in a weak signal for the most conservative sensitivity bound, but was stronger for the optimal bound, as seen in Figures 25, 26, 27.

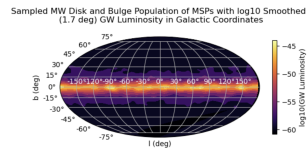


Figure 25: The GW signal for 1.7 degree angular resolution, with no sensitivity constraints enforced.

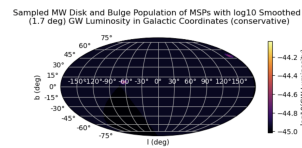


Figure 26: The GW signal for 1.7 degree angular resolution, with conservative sensitivity constraints enforced.

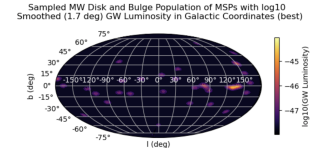


Figure 27: The GW signal for 1.7 degree angular resolution, with optimal sensitivity constraints enforced.

With an angular resolution of 10 degrees, both GW signals with conservative and optimal detector sensitivity constraints were visible. See Figures 28, 29, 30.

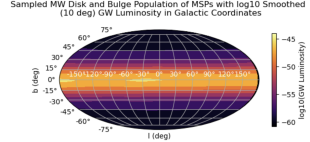


Figure 28: The GW signal for 10 degree angular resolution, with no sensitivity constraints enforced.

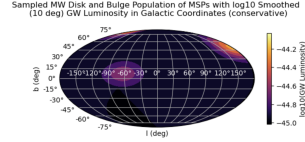


Figure 29: The GW signal for 10 degree angular resolution, with conservative sensitivity constraints enforced.

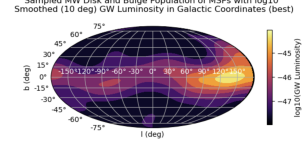


Figure 30: The GW signal for 10 degree angular resolution, with optimal sensitivity constraints enforced.

In addition to the GW luminosity morphology shown above, the number of detected MSPs, their corresponding averaged GW frequency, and their corresponding averaged GW luminosity were found for 50 variations on the MSP distribution for both detector sensitivity constraints. See Figures 31, 32, 33 for the conservative estimates and Figures 34, 35, 36 for the optimal estimates.

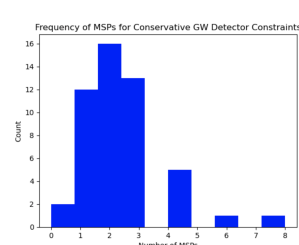


Figure 31: A histogram of the number of MSPs detectable for the most conservative GW detector sensitivity bounds.

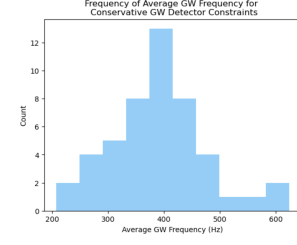


Figure 32: A histogram of the average GW frequency from detectable MSPs for the most conservative GW detector sensitivity bounds.

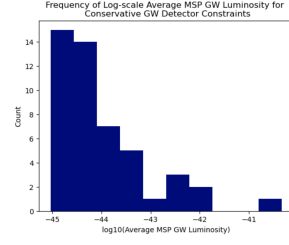


Figure 33: A histogram of the average GW luminosity from detectable MSPs for the most conservative GW detector sensitivity bounds.

For the most conservative GW detector sensitivity constraints, the average number of MSPs detectable was found to be 2. These MSPs had an average GW frequency of 391.88 Hz and an averaged GW luminosity of  $1.05 \times 10^{-42}$ .

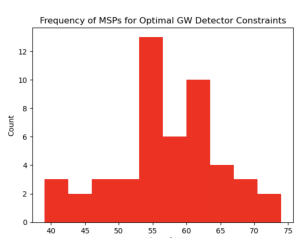


Figure 34: A histogram of the number of MSPs detectable for the most optimal GW detector sensitivity bounds.

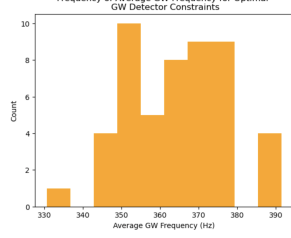


Figure 35: A histogram of the average GW frequency from detectable MSPs for the most optimal GW detector sensitivity bounds.

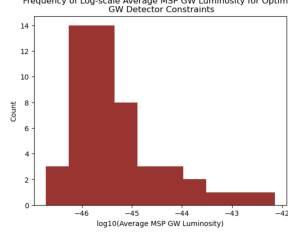


Figure 36: A histogram of the average GW luminosity from detectable MSPs for the most optimal GW detector sensitivity bounds.

For the most optimal GW detector sensitivity constraints, the average number of MSPs detectable was found to be 57. These MSPs had an average GW frequency of 364.29 Hz and an averaged GW luminosity of  $2.00 \times 10^{-44}$ .

## 6 Conclusion

In recent years we have entered an age of multi-messenger astronomy that has shown the ability that gravitational wave observatories have to understand astrophysical phenomenon in new ways. This new avenue of investigation into the universe has to potential to shed light on one of the enduring mysteries of high energy astrophysics: the galactic center excess. This source of gamma rays could be due to a yet unresolved population of millisecond pulsars located in the Milky Way disk and the nuclear bulge. Due to their rapid rotation and strong magnetic fields, millisecond pulsars are asymmetric about their axis of rotation, causing the emission of monochromatic gravitational waves. These can potentially be detected by current and future gravitational wave laser interferometers, as propagating gravitational waves cause differential motion of the interferometer arms, detected using the principle of interference.

Using MCMC and Inverse Transform methods, we generated a simulated population of approximately 40,000 millisecond pulsars and their corresponding ellipticities. We then generated the corresponding GW amplitude, luminosity, and frequency. Our results indicate that the gravitational wave frequency of a population of approximately 40,000 MSPs ranges from 2.3 to 3.5 in log space, or approximately 200 to 1400 Hz, owing to the relatively

high rotational frequency of most MSPs. This limits the detectability of our signal to GW detectors capable of probing high frequency signals such as TAMA, GEO, LIGO, Virgo, Kagra, and ET. Only Advanced LIGO/Virgo (with sensitivities above  $3 \times 10^{-23}$ ), Kagra (with sensitivities above  $10^{-23}$ ), and ET (with sensitivities above  $10^{-24}$ ) would be capable of detecting the GW signal, placing strong constraints on the morphology of the GW signal, the number of detectable MSPs, and the average GW frequency visible.

This suggests that if MSPs are responsible for the galactic center excess, then between 2–57 pulsars should be detectable, should have a corresponding GW frequency range of 364.29–391.88 Hz, and a corresponding GW luminosity range of  $2.00 \times 10^{-44}$ – $1.05 \times 10^{-42}$  given GW observatory’s sensitivity constraints. Therefore GW detectors sensitive to gravitational waves from MSPs and thus frequencies in the hundreds of hertz, must see at least a few MSPs, otherwise there are strong constraints placed on the abilities of MSPs to contribute to the galactic center excess.

In the future this analysis could be further strengthened by performing a robust statistical analysis of the parameter space and the possibility of detection. It would also be interesting to explore the impact of a time-dependent ellipticity distribution on the strength and detectability of the GW signal. Additionally, it could be that the galactic center excess is caused by a combination of MSPs and annihilating dark matter, so it would be illuminating to incorporate that scenario into the current model and distribution of MSPs and to evaluate the resulting GW signal.

## 7 Acknowledgements

I would like to thank my advisor Stefano Profumo for his support and guidance during the duration of this project. His advice and suggestions were indispensable. I would also like to thank N.G. and E.S. for giving their feedback, comments, and advice on this project.

## 8 References

- [1] J Aasi et al. “Advanced LIGO”. In: *Classical and Quantum Gravity* 32.7 (Mar. 2015), p. 074001. ISSN: 1361-6382. DOI: 10.1088/0264-9381/32/7/074001. URL: <http://dx.doi.org/10.1088/0264-9381/32/7/074001>.
- [2] B P Abbott et al. “LIGO: the Laser Interferometer Gravitational-Wave Observatory”. In: *Reports on Progress in Physics* 72.7 (June 2009), p. 076901. ISSN: 1361-6633. DOI: 10.1088/0034-4885/72/7/076901. URL: <http://dx.doi.org/10.1088/0034-4885/72/7/076901>.
- [3] B. P. Abbott et al. “GW170817: Observation of Gravitational Waves from a Binary Neutron Star Inspiral”. In: *Physical Review Letters* 119.16 (Oct. 2017). ISSN: 1079-7114. DOI: 10.1103/physrevlett.119.161101. URL: <http://dx.doi.org/10.1103/PhysRevLett.119.161101>.
- [4] F Acernese et al. “Advanced Virgo: a second-generation interferometric gravitational wave detector”. In: *Classical and Quantum Gravity* 32.2 (Dec. 2014), p. 024001. ISSN: 1361-6382. DOI: 10.1088/0264-9381/32/2/024001. URL: <http://dx.doi.org/10.1088/0264-9381/32/2/024001>.
- [5] Deepali Agarwal et al. “Targeted search for the stochastic gravitational-wave background from the galactic millisecond pulsar population”. In: *Physical Review D* 106.4 (Aug. 2022). ISSN: 2470-0029. DOI: 10.1103/physrevd.106.043019. URL: <http://dx.doi.org/10.1103/PhysRevD.106.043019>.
- [6] Masaki Ando et al. “Stable Operation of a 300-m Laser Interferometer with Sufficient Sensitivity to Detect Gravitational-Wave Events within Our Galaxy”. In: *Physical Review Letters* 86.18 (Apr. 2001), pp. 3950–3954. ISSN: 1079-7114. DOI: 10.1103/physrevlett.86.3950. URL: <http://dx.doi.org/10.1103/PhysRevLett.86.3950>.
- [7] Yoichi Aso et al. “Interferometer design of the KAGRA gravitational wave detector”. In: *Physical Review D* 88.4 (Aug. 2013). ISSN: 1550-2368. DOI: 10.1103/physrevd.88.043007. URL: <http://dx.doi.org/10.1103/PhysRevD.88.043007>.
- [8] John Baker et al. *High angular resolution gravitational wave astronomy*. 2019. arXiv: 1908.11410 [astro-ph.HE].

- [9] Malte Buschmann et al. “Foreground mismodeling and the point source explanation of the Fermi Galactic Center excess”. In: *Physical Review D* 102.2 (July 2020). ISSN: 2470-0029. DOI: 10.1103/physrevd.102.023023. URL: <http://dx.doi.org/10.1103/PhysRevD.102.023023>.
- [10] Wen-Cong Chen. “Constraining the ellipticity of millisecond pulsars with observed spin-down rates”. In: *Physical Review D* 102.4 (Aug. 2020). ISSN: 2470-0029. DOI: 10.1103/physrevd.102.043020. URL: <http://dx.doi.org/10.1103/PhysRevD.102.043020>.
- [11] K L Dooley. “Status of GEO 600”. In: *Journal of Physics: Conference Series* 610 (May 2015), p. 012015. ISSN: 1742-6596. DOI: 10.1088/1742-6596/610/1/012015. URL: <http://dx.doi.org/10.1088/1742-6596/610/1/012015>.
- [12] Christopher Eckner et al. “Millisecond Pulsar Origin of the Galactic Center Excess and Extended Gamma-Ray Emission from Andromeda: A Closer Look”. In: *The Astrophysical Journal* 862.1 (July 2018), p. 79. ISSN: 1538-4357. DOI: 10.3847/1538-4357/aac029. URL: <http://dx.doi.org/10.3847/1538-4357/aac029>.
- [13] Daniel Foreman-Mackey et al. “`emcee`: The MCMC Hammer”. In: *Publications of the Astronomical Society of the Pacific* 125.925 (Mar. 2013), pp. 306–312. ISSN: 1538-3873. DOI: 10.1086/670067. URL: <http://dx.doi.org/10.1086/670067>.
- [14] Lisa Goodenough and Dan Hooper. *Possible Evidence For Dark Matter Annihilation In The Inner Milky Way From The Fermi Gamma Ray Space Telescope*. 2009. arXiv: 0910.2998 [hep-ph].
- [15] Ian Holst and Dan Hooper. *A New Determination of the Millisecond Pulsar Gamma-Ray Luminosity Function and Implications for the Galactic Center Gamma-Ray Excess*. 2024. arXiv: 2403.00978 [astro-ph.HE].
- [16] Nuutti Hyvonen. *Computational methods in inverse problems*. 2011. URL: <https://users.aalto.fi/~nhyvonen/Lectures/cmip.pdf>.
- [17] Rebecca K. Leane and Tracy R. Slatyer. “Spurious Point Source Signals in the Galactic Center Excess”. In: *Physical Review Letters* 125.12 (Sept. 2020). ISSN: 1079-7114. DOI: 10.1103/physrevlett.125.121105. URL: <http://dx.doi.org/10.1103/PhysRevLett.125.121105>.

- [18] Rebecca K. Leane and Tracy R. Slatyer. “The enigmatic Galactic Center excess: Spurious point sources and signal mismodeling”. In: *Physical Review D* 102.6 (Sept. 2020). ISSN: 2470-0029. DOI: 10.1103/physrevd.102.063019. URL: <http://dx.doi.org/10.1103/PhysRevD.102.063019>.
- [19] Oscar Macias et al. “Galactic bulge preferred over dark matter for the Galactic centre gamma-ray excess”. In: *Nature Astronomy* 2.5 (Mar. 2018), pp. 387–392. ISSN: 2397-3366. DOI: 10.1038/s41550-018-0414-3. URL: <http://dx.doi.org/10.1038/s41550-018-0414-3>.
- [20] Oscar Macias et al. “Strong evidence that the galactic bulge is shining in gamma rays”. In: *Journal of Cosmology and Astroparticle Physics* 2019.09 (Sept. 2019), pp. 042–042. ISSN: 1475-7516. DOI: 10.1088/1475-7516/2019/09/042. URL: <http://dx.doi.org/10.1088/1475-7516/2019/09/042>.
- [21] R. N. Manchester et al. “The Australia Telescope National Facility Pulsar Catalogue”. In: *The Astronomical Journal* 129.4 (Apr. 2005), pp. 1993–2006. ISSN: 1538-3881. DOI: 10.1086/428488. URL: <http://dx.doi.org/10.1086/428488>.
- [22] Andrew L. Miller and Yue Zhao. “Probing the Pulsar Explanation of the Galactic-Center GeV Excess Using Continuous Gravitational-Wave Searches”. In: *Physical Review Letters* 131.8 (Aug. 2023). ISSN: 1079-7114. DOI: 10.1103/physrevlett.131.081401. URL: <http://dx.doi.org/10.1103/PhysRevLett.131.081401>.
- [23] C J Moore, R H Cole, and C P L Berry. “Gravitational-wave sensitivity curves”. In: *Classical and Quantum Gravity* 32.1 (Dec. 2014), p. 015014. ISSN: 1361-6382. DOI: 10.1088/0264-9381/32/1/015014. URL: <http://dx.doi.org/10.1088/0264-9381/32/1/015014>.
- [24] Harrison Ploeg. *The Galactic Millisecond Pulsar Population: Implications for the Galactic Center Excess*. 2021. arXiv: 2109.08439 [astro-ph.HE].
- [25] Samuel Rowlinson et al. “Feasibility study of beam-expanding telescopes in the interferometer arms for the Einstein Telescope”. In: *Physical Review D* 103.2 (Jan. 2021). ISSN: 2470-0029. DOI: 10.1103/physrevd.103.023004. URL: <http://dx.doi.org/10.1103/PhysRevD.103.023004>.

- [26] Magdalena Sieniawska and David Ian Jones. “Gravitational waves from spinning neutron stars as not-quite-standard sirens”. In: *Monthly Notices of the Royal Astronomical Society* 509.4 (Nov. 2021), pp. 5179–5187. ISSN: 1365-2966. DOI: 10.1093/mnras/stab3315. URL: <http://dx.doi.org/10.1093/mnras/stab3315>.
- [27] Tracy Slatyer. “Les Houches Lectures on Indirect Detection of Dark Matter”. In: *SciPost Physics Lecture Notes* (May 2022). ISSN: 2590-1990. DOI: 10.21468/scipostphyslectnotes.53. URL: <http://dx.doi.org/10.21468/SciPostPhysLectNotes.53>.
- [28] Emma Storm, Christoph Weniger, and Francesca Calore. “SkyFACT: high-dimensional modeling of gamma-ray emission with adaptive templates and penalized likelihoods”. In: *Journal of Cosmology and Astroparticle Physics* 2017.08 (Aug. 2017), pp. 022–022. ISSN: 1475-7516. DOI: 10.1088/1475-7516/2017/08/022. URL: <http://dx.doi.org/10.1088/1475-7516/2017/08/022>.
- [29] G. Woan et al. “Evidence for a Minimum Ellipticity in Millisecond Pulsars”. In: *The Astrophysical Journal Letters* 863.2 (Aug. 2018), p. L40. ISSN: 2041-8213. DOI: 10.3847/2041-8213/aad86a. URL: <http://dx.doi.org/10.3847/2041-8213/aad86a>.
- [30] Qiang Yuan and Bing Zhang. “Millisecond pulsar interpretation of the Galactic center gamma-ray excess”. In: *Journal of High Energy Astrophysics* 3–4 (Sept. 2014), pp. 1–8. ISSN: 2214-4048. DOI: 10.1016/j.jheap.2014.06.001. URL: <http://dx.doi.org/10.1016/j.jheap.2014.06.001>.